Investigations of the eye fundus using a simultaneous optical coherence tomography/indocyanine green fluorescence imaging system

Adrian G. Podoleanu
George M. Dobre
Ramona Cernat
University of Kent at Canterbury
Applied Optics Group
School of Physical Sciences
Canterbury CT2 7NH
United Kingdom
E-mail: ap11@kent.ac.uk

John A. Rogers
Justin Pedro
Ophthalmic Technologies Inc.
37 Kodiak Cres Unit 16
Toronto, Ontario M3J 3E5 Canada

Richard B. Rosen
Patricia Garcia
The New York Eye and Ear Infirmary
Advanced Retinal Imaging Center
310 East 14th Street
New York, New York 10003-4297

Abstract. We develop a dual-channel optical coherence tomography/indocyanine green (OCT/ICG) fluorescence system based on our previously reported ophthalmic OCT/confocal imaging system. The confocal channel is tuned to the fluorescence wavelength range of the ICG dye and light from the same optical source is used to generate the OCT image and to excite the ICG fluorescence. The system enables the clinician to visualize simultaneously *en face* OCT slices and corresponding ICG angiograms of the ocular fundus, displayed side by side. C-scan (constant depth) and B-scan (cross section) images are collected by fast *en face* scanning (T-scan). The pixel-to-pixel correspondence between the OCT and angiography images enables the user to precisely capture OCT B-scans at selected points on the ICG confocal images. © *2007 Society of Photo-Optical Instrumentation Engineers.* [DOI: 10.1117/1.2434970]

1 Introduction

Fluorescence of indocyanine green (ICG) dye is an established technique used in ophthalmic investigations of blood circulation through the choroid of the eye. It has become increasingly important in ophthalmology over the last few decades, whether in the form of the more recently developed scanning laser angiography[1] or in the more conventional guise of digital fundus camera fluorescence photography.[2] The near-IR light absorbed by ICG, as well as its fluorescent emission, could more easily penetrate normal ocular pigments such as melanin and xantophyll; the human retinal pigment epithelium (RPE) and choroid absorb between 59 and 75% of the light in the blue-green range at a wavelength of approximately 500 nm, but only 21 to 38% of near-IR light[3] at 800 nm. ICG is a well-tolerated drug and the IR light is known to be less harmful than shorter wavelength light with respect to causing phototoxic effects in the retina.

Often, the angiography investigation will reveal areas of abnormal vascular leakage that will require higher resolution cross-sectional and tomographic imaging of the retina to clarify the pathology; the patient may then require subsequent optical coherence tomography (OCT) imaging.[4,5]

OCT uses an interferometer with a low-coherence source whose spectral width determines the depth resolution. Broader spectra give better, narrower depth resolutions. Using combinations of superluminescent diodes, depth resolutions of better than 2 μm can be obtained, while using a Kerr lens mode-locked laser, photonic crystal fiber, or tapered fiber, a resolution close to 1 μm was recently reported.[6] In this paper, we describe the system that for the first time produced simultaneous ICG fluorescence and OCT images of the eye fundus. On one hand, ICG angiography and OCT appear well suited to operate together because they share similar spectral bands. The most widely used band for retinal OCT of the retina is 820 to 920 nm, where the main constituents in the eye, such as photopigments and water, exhibit low absorption.[7] ICG is usually excited around 790 to 810 nm and fluoresces in the band 810 to 860 nm with a peak at 830 nm, as shown in Figs. 1 and 2.[8,9] Operating in similar bands enables the same source to be used for ICG excitation as well as for the production of an OCT image. On the other hand, the proximity of the excitation wavelength to the fluorescence band raises several optimization issues, as presented in the following.

The fluorescent light is incoherent with respect to the excitation signal and therefore the OCT channel is insensitive to the fluorescent light.

2 Instrument

The instrument, presented in schematic diagram in Fig. 3, is a dual-channel OCT/confocal ophthalmoscope[10,11] with versatile scanning and image display capabilities, enabling the acquisition of pairs of OCT and confocal images in the B- or

Address all correspondence to Adrian Podoleanu, School of Physical Sciences, University of Kent–Canterbury, Kent CT2 7NH, United Kingdom; Phone: +44 1227 823272; Fax: +44 1227 827558; E-mail: apiii@kent.ac.uk
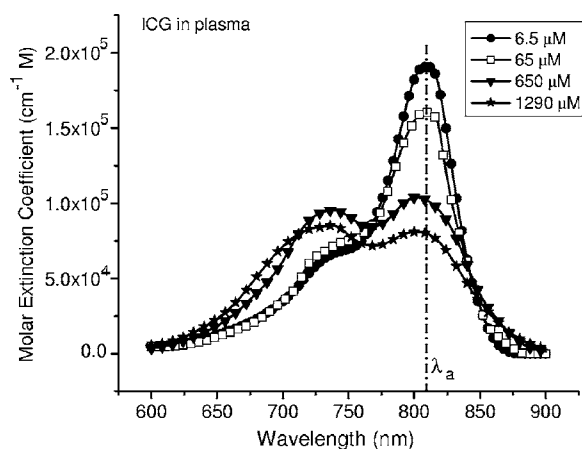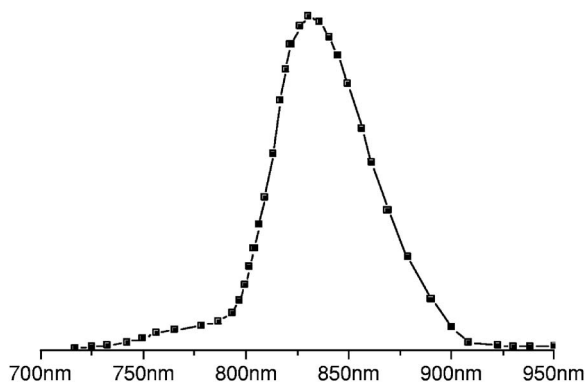
Fig. 1 Plot of the molar extinction coefficient of ICG in plasma against wavelength for different ICG concentrations in plasma. Replotted from data (http://omlc.ogi.edu/spectra/icg/), interpolated by Scott Prahl based on Ref. 8.

C-scan regime of operation.[12] The image in the OCT channel is created by using the phase modulation created by the transverse scanner.[13] The splitter used in the OCT/ophthalmoscope configuration[14] to divert some of the light to a separate confocal receiver was replaced in this implementation by a chromatic splitter (CS). This separates the retina-scattered light at the excitation wavelength, guided into the OCT channel, from the fluorescence signal, conveyed toward the confocal receiver.[15] To enhance the contrast of fluorescence in the confocal receiver, a fluorescence emission filter is used in the fluorescence channel to attenuate the residual amount of excitation light transmitted through the CS filter.

3 Challenges Arising from the Combination of OCT with Fluorescence Imaging in the Same System

The depth resolution achievable in OCT is determined by the profile of the correlation function of the source used. The depth resolution is generally worse than the width of the correlation function due to dispersion that is left uncompensated in the low-coherence interferometer, therefore careful attention is paid in matching the length of different optical materials in the two arms of the interferometer. Simultaneous operation of OCT with collection of fluorescence requires spectral filters, such as cold, hot mirrors or dichroic filters. The mere introduction of such a filter in the interferometer deteriorates the correlation profile in two respects: (1) it widens the main lobe and (2) it introduces secondary lobes, which determine ghosts in depth in the OCT image. Therefore, the slope of transition from low to high transmission versus wavelength, as well as the threshold wavelength (the point where the transmission is half of the maximum) must be designed in such a way as to minimize the deterioration of the correlation profile.

On the other hand, because the source used has a large bandwidth, its spectral wings extend toward the fluorescence band and the longer wavelength part of the source spectrum must be attenuated, otherwise weak fluorescence would not be recognized out of the background. Consequently, collection of fluorescence cannot start too close to the central wavelength of the source, as is the case in angiography systems using lasers for the ICG excitation. This leads to a reduction in the amount of fluorescence collected by an OCT/ICG system in comparison to a laser angiograph. Therefore, a trade-off must be found between the amount of fluorescence light rejected and the source bandwidth that determines the depth resolution.

4 Design Considerations

The spectral separation of the OCT signal from the fluorescence signal returned by the target is performed by the CS, whose transition wavelength λ_{tr} must be carefully selected to fall between the bulk of the OCT light and the fluorescence emission band. Therefore, the most important step on the way to OCT/fluorescence integration is to determine the most appropriate choice and match of filters and optical source parameters (central wavelength and bandwidth), which is discussed in the following.

4.1 Chromatic Splitter

Two goals were pursued simultaneously in the choice of a CS filter: to achieve (1) a good depth resolution in the OCT channel as well as (2) an appropriate brightness and contrast for the images delivered by the fluorescence channel. The depth resolution capability of the OCT channel is determined by the FWHM of the main lobe of the autocorrelation function, as well as by its shape, with a nearly Gaussian spectrum being the most desirable. The sensitivity of the fluorescence channel is determined by balancing the best rejection of excitation light leaked into the fluorescence channel with the minimization of losses of the genuine fluorescent signal. Several parameters play a critical role in how well these aims are met: the central operating wavelength of the light source λ_c, the width of its spectrum $\Delta\lambda$, the CS transition wavelength λ_{tr}, the reflectivity of the filter for the OCT band R_{OCT}, and the transmission of the filter for the fluorescence band T_F. The CS was employed in reflection for the OCT signal and in transmission for the fluorescence signal. Alternatively, the filter could have been used in transmission by the OCT channel and in reflection by the fluorescence channel. The advantage of having the CS reflect OCT light was that it avoided the ne-
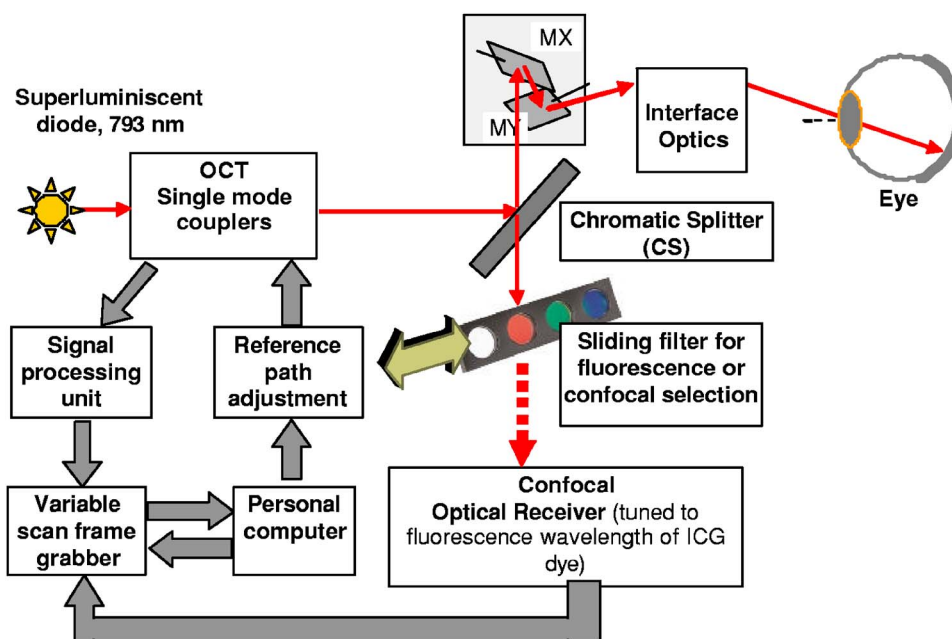

Fig. 2 ICG fluorescence spectrum (data points obtained from Fig. 2 in Ref. 9 and curve redrawn).

Fig. 3 General setup of the combined OCT/ICG-confocal system: MX and MY, galvanometer mirrors of the *XY* scanning pair.

cessity to compensate for the material dispersion of the filter substrate, essential in achieving a narrow sampling function in depth.

The optimization of system performance in relation to the optical source and the CS filter was performed using a titanium:sapphire laser (Coherent "Mira-Seed," wavelength tunable between 780 and 850 nm). The adjustable wavelength feature of the Mira-Seed laser was particularly attractive for our investigations in the quest for the most optimal set of parameters, wavelength and source bandwidth. By varying the launching into single-mode fiber, we obtained variable linewidth $\Delta\lambda$ between 30 and 70 nm.

The behavior of OCT light was assessed for four laser operating wavelengths λ_c, namely, 780, 800, 820, and 840 nm. The autocorrelation function in the OCT channel at each of these wavelengths was measured after reflection on each of four filters, with transition wavelengths $\lambda_{tr}=795$, 805, 810, and 820 nm. A bulk zero-dispersion Michelson interferometer was used to evaluate the correlation function for the light reflected by the CS.

We tested different combinations of filters and central wavelengths and detail here the results for one such pair, laser wavelength $\lambda_c=780$ nm and a CS filter with $\lambda_{tr}=795$ nm. CS is a cold mirror with a transition wavelength λ_{tr} between the excitation band and the fluorescence band. The steeper the CS transition profile from high to low reflectance, and the closer λ_{tr} is to the excitation wavelength λ_c, the more distorted the correlation profile becomes. Two characteristics can be used to quantify this distortion: (1) the enlargement of the main lobe (which leads to worse depth resolution) and (2) ripple, leading to ghosts in the OCT image.

The spectral makeup of light from the Mira-Seed, tuned to $\lambda_c=780$ nm at the output of a 3 km reel of single-mode (SM) fiber is shown in Fig. 4(a), together with the transmission curve of the $\lambda_{tr}=795$ nm CS. The curves for the other split-

ters in the set are quite similar. Reflection at CS results in a substantially modified spectrum, as shown in Fig. 4(b), which determines the shape of the autocorrelation function in the OCT channel, shown in Fig. 4(c).

The 3-km-long SM fiber had a substantial effect on broadening the original spectrum of the Mira-Seed output, which in a stand-alone OCT system would lead to a depth resolution of better than 5 μm. The subsequent reflection of the light at the CS filter resulted in a seriously distorted spectral shape. A coherence signature like the one shown in Fig. 4(c), exhibiting satellite peaks, was the result.

Overall, the least distorted spectra and the smallest autocorrelation satellite peaks were obtained for the maximum separation between λ_c and λ_{tr}. However, their separation should not be too large. The requirement to maintain the band above 800 nm free of OCT excitation light and available for the detection of fluorescence (see Figs. 1 and 2) suggests that the optimal trade-off is achieved when the central wavelength λ_c is kept below 795 nm and λ_{tr} is around 805 to 810 nm. An increase in λ_c and λ_{tr} over these values while maintaining some distance between them will lead to stray signal in the fluorescence channel as well as to a reduction in the fluorescence collection, while a decrease of λ_c below 795 nm will lead to a reduction in the ICG excitation, as explained as follows.

4.2 *SLD Sources versus Broader Band Sources*

A clear separation between the OCT/excitation light and the fluorescence band has the advantage of maintaining superior contrast in the fluorescence image. However, increasing the separation between the excitation wavelength and the peak of absorption at $\lambda_a=806$ nm has the effect of decreasing the excitation efficiency of the fluorophore. The current superluminescent diode (SLD) technology is limited in optical power
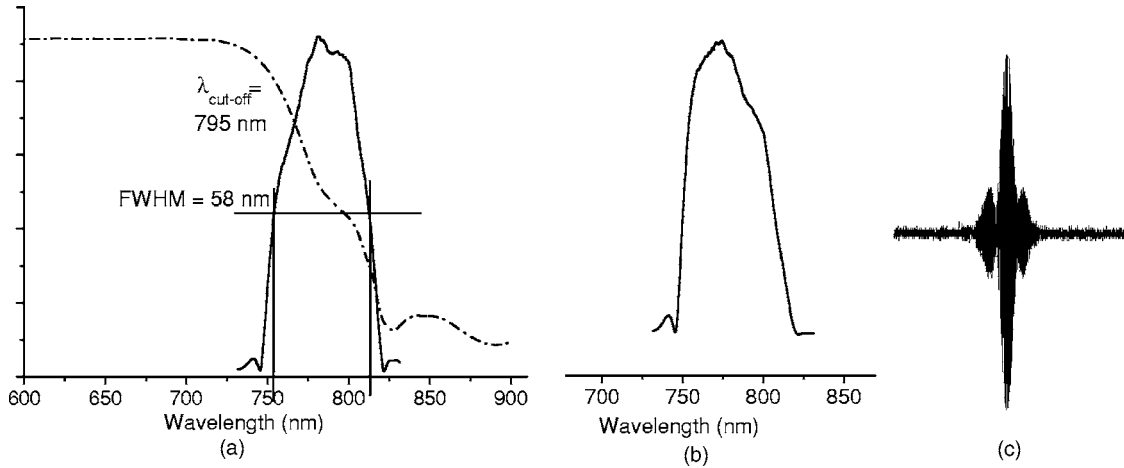
Fig. 4 (a) Spectrum of $\lambda_c = 780$ nm Mira-speed output after propagation through a 3-km-long SM fiber, prior to incidence on the CS (continuous line) and transmission of the CS filter (dashed line); (b) same light after undergoing reflection at CS with $\lambda_{cut\text{-}off} = \lambda_{tr} = 795$ nm; and (c) autocorrelation function for the light reflected at CS, measured with a low dispersion bulk Michelson interferometer.

output, while this is not a limitation for broadband Ti:Sa lasers[16] currently employed in high-resolution OCT.

### 4.3 Source Spectrum Width versus CS Steepness

Figures 5(a) and 5(b) show two source spectra centered at the same central wavelength of 790 nm but with different FWHMs, of 10 and 100 nm, respectively, in comparison to the spectral reflectivity profile of a cold mirror produced by Chroma, which is displayed in these figures for illustration. Figure 5(a) shows a case where the source bandwidth is comparable with the CS transition width, while Fig. 5(b) shows a case where the bandwidth is wider than the transition width. The signal that reaches the target and the signal returned to the photodetector depend on the relative position of the central wavelength to the CS transition region, on the steepness of the CS filter curve, and on the source bandwidth. The central wavelength is placed in the middle of the transition range of the filter in Fig. 5, which as explained in the previous section will lead to severe distortions of the OCT depth sampling profile.

Because of the double reflection taking place at CS, the efficiency of producing the OCT signal can be expressed as

$$\eta = \frac{\int SR^2 d\lambda}{\int S\, d\lambda},\qquad(1)$$

where R is the reflectivity characteristic of the CS, and S is the Gaussian spectral power density of the source. The efficiency η was calculated and is represented in the graph in Fig. 6.

For a central source wavelength λ_c lower than 780 nm, the efficiency and the source bandwidth are in an inverse proportionality relationship because for wider spectra there will be wavelengths extending to regions with reduced CS reflectivity. For central wavelengths smaller than 780 nm, the efficiency increases as one of the source spectral wings extends over regions of higher CS reflectivity. Calculation for wavelengths longer than 810 nm was not carried out as this would fall into the fluorescence spectrum. The graphs in Fig. 6 show that the choice of wavelength is more critical for a narrow-bandwidth source, such as an SLD, than for a large bandwidth source, such as a white light source. For an SLD whose typi-
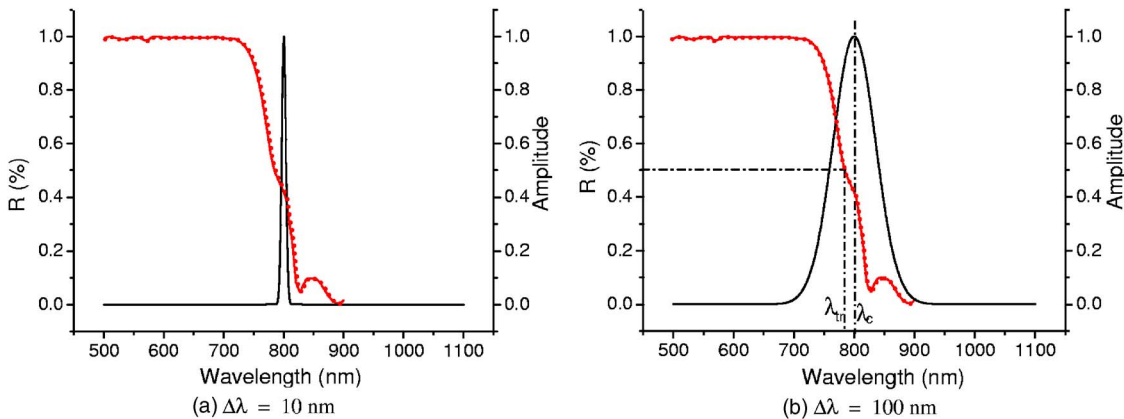
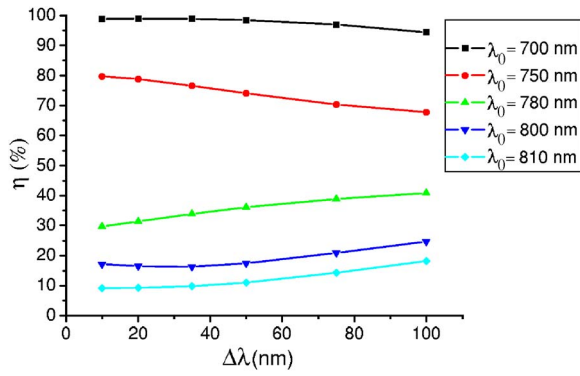**Fig. 5** Superposition of the CS reflectivity curve and the source spectrum with different FWHM $\Delta\lambda$.

Fig. 6 Efficiency η in generating the OCT signal.

Fig. 7 Graphs used in calculation of the ICG excitation efficiency; *A*, ICG absorption spectrum; *S*, SLD spectrum; *R*, CS reflectivity spectrum.

cal bandwidth is less than 30 nm, the efficiency decreases from maximum to 10% when the central wavelength is increased from 700 to 810 nm.

4.4 Efficiency in Fluorescence Excitation

Figure 1 shows the absorption spectrum of ICG in plasma.[8] This exhibits a peak at $\lambda_a = 806$ nm, and ideally, λ_c should be as close as possible to this value. As mentioned, to reduce the enlargement of the main lobe and the ripple of the correlation function, a sufficient gap between λ_{tr} and λ_c is sought. Note that λ_{tr} must separate the optical source spectrum and the fluorescence spectrum, therefore, $\lambda_c \approx \lambda_a > \lambda_{tr} > \lambda_{cut-off}$. The value of $\lambda_{cut-off}$ represents the minimum value of wavelength where the fluorescence spectrum is cut off by the CS filter. This may extend into the ICG fluorescence spectrum. As seen in Fig. 2, the fluorescence spectrum extends significantly over the absorption spectrum in Fig. 1, which explains the difficulty in separating the excitation from fluorescence when using ICG angiography. It is even more difficult to separate these bands when a low-coherence source is used. We may therefore select $\lambda_{fl,min} = 815$ nm. As $\lambda_a = 806$ nm, this allows only a small wavelength interval for λ_{tr}, which leads to an abrupt transition required for the CS filter. To reduce the slope of the CS filter, we can move λ_c to smaller values within the absorption spectrum in Fig. 1, at the expense of the efficiency in exciting the fluorescence. To evaluate this efficiency, the ICG absorption spectrum, SLD spectrum, and CS reflectivity are shown superposed in Fig. 7 for an arbitrary value of $\lambda_c < \lambda_a$, where *S* is the source spectrum, *R* is the reflection spectrum of the CS, and *A* is the ICG absorption spectrum. All spectra are normalized. The excitation of the ICG can be evaluated by

$$\varepsilon_{excit} = \frac{\int SRA d\lambda}{\int A d\lambda}. \qquad (2)$$

The definition of the ICG excitation efficiency in Eq. (2) differs from that of OCT excitation defined in Eq. (1) by the incorporation of the absorption spectrum *A* factor. Using Eq. (2), the graphs in Fig. 8 were obtained, which show that for the given CS curve, efficiencies below 0.2 are achievable with SLDs of $\Delta\lambda$ below 35 nm. For maximum efficiency, the cen-
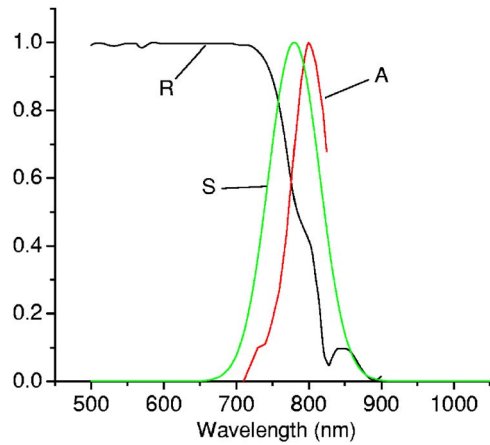
tral wavelength, λ_c should be as close as possible to the ICG absorption peak, at λ_a, as shown by the graphs for $\lambda_c = 780$ and 800 nm. Enlarging the bandwidth of the source up to 100 nm doubles the efficiency value.

We performed optimization of these parameters and found that by shifting the excitation wavelength from the optimum of 806 to 793 nm, in combination with a CS with $\lambda_{tr} = 795$ nm, which has 90% transmission at 815 nm and reflection close to 95% at 793 nm, the correlation function experiences little distortion. The choice of $\lambda_c = 793$ nm was also determined by advances in the SLD technology. This enabled Superlum Moscow to produce a comparatively powerful SLD for this project, with a 5-mW *ex fiber* and $\Delta\lambda = 21.6$ nm spectral FWHM, which determines a depth resolution in the tissue of 11 μm (considering an index of refraction in the retina *n* ~ 1.4).

4.5 Confocal Receiver Fluorescence Sensitivity

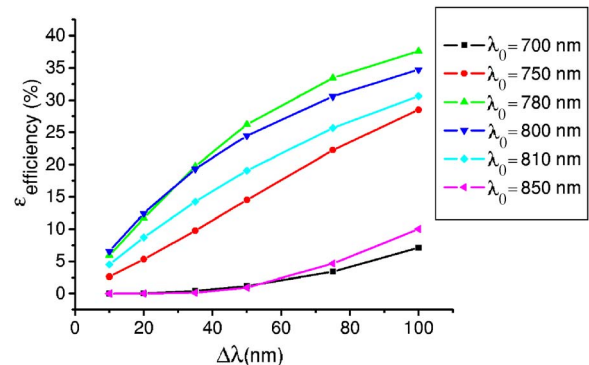How much of the fluorescence spectrum is conveyed to the confocal receiver is found by evaluating

Fig. 8 Efficiency in the excitation of the ICG versus the optical source bandwidth for different values of the central wavelength.
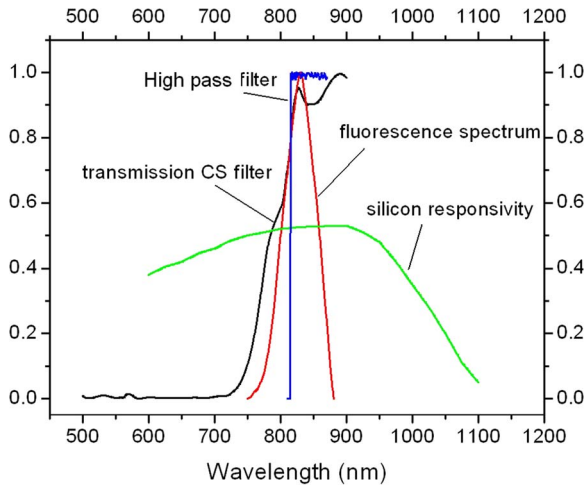
Fig. 9 Spectra involved in the evaluation of efficiency in capturing the fluorescence signal.

$$\varepsilon_F = \frac{\int F_{em}(1-R)T_F \mathrm{Si}\, d\lambda}{\int F_{em}\, d\lambda}, \qquad (3)$$

where F_{em} is the normalized fluorescence spectrum, R is the CS reflection spectrum, T_F is the transmission of the fluorescence filter, and Si is the silicon responsivity of the photodetector. Figure 9 represents these contributions, where as fluorescence filter, a highpass filter with a relatively steep transition (LPF812 manufactured by Iridian Canada) was used. Here the filter can exhibit a steep transition because it is in the confocal path. A steeper transition naturally results in a better rejection of excitation light and better transmission for the fluorescent light. Without the filter, the efficiency is $\varepsilon_F = 0.43$ A/W, while using it, a value of $\varepsilon_F = 0.33$ A/W results. This value should also be multiplied with the efficiency of launching light into the confocal receiver, which is ≈ 0.3 in our experimental implementation.

4.6 Stray Fluorescence in the Confocal Channel

Another important parameter is the amount of stray fluorescence leaking into the confocal channel from the optical source, p:

$$P = \frac{\int_{\lambda_{min\,F}}^{\lambda_{max\,F}} T_F SR(1-R)\, d\lambda}{\int SRA\, d\lambda}, \qquad (4)$$

where $\lambda_{min,F}$ and $\lambda_{max,F}$ represent the margins of the fluorescence spectrum, 805 to 900 nm. Stray fluorescence contributes to output of the fluorescence channel and prevents observation of deep thin vessels in the choroid. For the CS having the profile R, as shown in Fig. 7, stray fluorescence versus $\Delta\lambda$ was calculated and the resulting graphs are presented in Fig. 10. Deliberately, the factor T_F in Eq. (4) was not considered in obtaining these graphs in order to evaluate the capability of
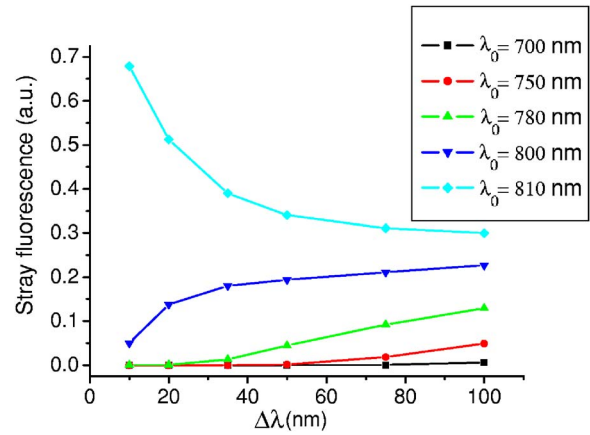

Fig. 10 Stray reflectance in the confocal channel.

the configuration on its own in rejecting the stray fluorescence. For an SLD centered at $\lambda_c = 780$ nm, the stray fluorescence with $\Delta\lambda = 100$ nm is 50 times larger than for an SLD source with $\Delta\lambda = 30$ nm. If the central wavelength is too close to the fluorescence band, then the stray fluorescence is large irrespective of $\Delta\lambda$, as expected.

5 Results

The acquisition of fluorescent images has to proceed rapidly, in less than a minute, due to the fast ICG disappearance rate from the blood stream of between 18 and 24% per minute.[17,18] Generating pairs of OCT and ICG images at 2 Hz enabled the production of OCT images of a high enough quality. This rate, however, may not be sufficiently fast for the acquisition of images of important stages in the ICG transit. Following the injection of ICG solution into the patient's bloodstream (5 mg/ml), light from the SLD guided through to the eye fundus by means of the interface optics, (1) generates a reflected/backscattered return at the same wavelength (793 nm) which coherently combines with reference light to produce the OCT images, and (2) serves to excite fluorescence in any tissue structures containing the ICG dye contrast agent, such as retinal and choroidal blood vessels.

The 12-bit gray-scale images in the two channels are displayed simultaneously side-by-side. Figure 11, shows such pairs of images, the OCT (right) and ICG fluorescence (left) containing the fovea and optic nerve of a healthy eye, taken at different times in the postinjection phase. In 30 s, 60 such pairs are acquired while the depth is explored over a range of typically 1.2 mm in retinal tissue. Two examples of ICG/OCT pairs from a much longer series are shown in Fig. 11, at different times and at different arbitrary depths. If the eye has moved considerably during the acquisition and essential parts from the retina volume are missing, the acquisition can be repeated after the ICG bolus has passed. The pixel-to-pixel correspondence between the two images in the pair enables later association of morphologic features between the two images. Generally, just a few correct *en face* OCT images from the stack collected during the bolus passage are sufficient for subsequent transverse alignment of any other pairs of images.

(a)

(b)
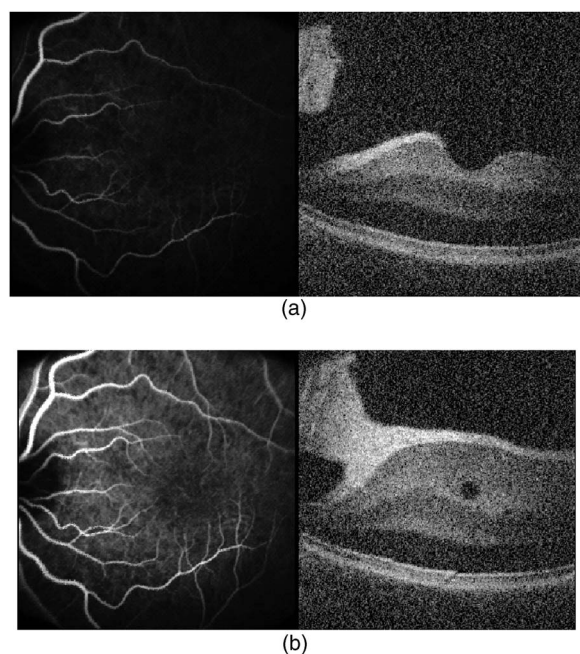
Fig. 11 *En face* OCT (right) and ICG fluorescence (left) images of the eye fundus of a healthy volunteer in the postinjection phase at (a) 15 s, showing early retinal arteriolar filling, and (b) 20 s, showing full arteriolar and venular filling of the left eye. The OCT images demonstrate a slight downward tilt of the eye, which causes the slices to include the vitreous at the top of the frame and the choroid at the bottom. Lateral size, 4 × 4 mm.

6 Eyes with Pathology

Figures 12(a) and 12(b) present pairs of images from an eye with a choroidal neovascular membrane. The confocal fluorescence image on the left reveals the location of active leakage within the lesion.

(a)   (b)

(c)
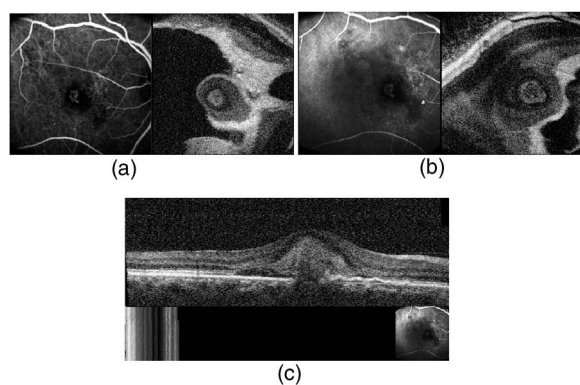
Fig. 12 *En face* OCT (right) and ICG fluorescence (left) images of the right fundus of a patient with a well-defined classic choroidal neovascular membrane in the post-injection phase at (a) 10 s and (b) 15 s. The ICG images highlight the vascular component of the membrane, while the accompanying OCT images reveal the surrounding serous retinal elevation. Lateral size, 4 × 4 mm. (c) Longitudinal OCT image of the fundus of a patient with a choroidal neovascular membrane. The image demonstrates the defect in the RPE layer through which the vascular lesion has grown. The insets show: left, confocal image during acquisition of the B-scan and right, confocal C-scan image immediately prior to switching the system from C- to B-scan.

(a)   (b)

(c)
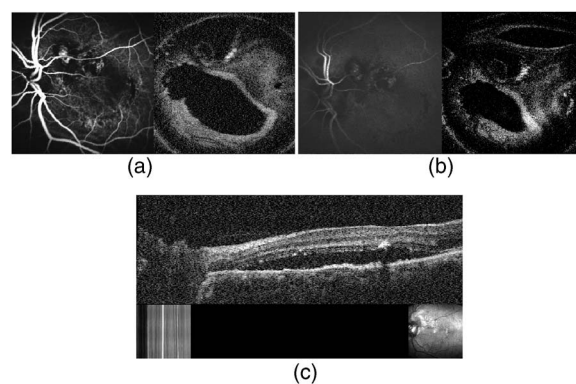
Fig. 13 *En face* OCT (right) and ICG fluorescence (left) images of the fundus of a patient with a polypoidal choroidal vasculopathy in the post-injection phase at (a) 50 s and (b) 300 s. The three bright vascular lesions seen in (a) fade in (b) demonstrating lack of leakage. The black oval in the middle of the OCT images represents a serous elevation of the neurosensory retina which can be seen in cross-section in (c). The smaller bright oval above is a detachment of the retinal pigment epithelium surrounding the region of the vascular "polyps." (c) Longitudinal OCT image of the fundus of a patient with polypoidal choroidal vasculopathy. The insets show: left, confocal scan lines during acquisition of the B-scan and right, confocal C-scan image immediately prior to switching the system from C- to B-scan. The scan lines are useful to help the interpreter determine the extent of movement artifact in the OCT image. This cross section is taken through serous elevation of the retina adjacent and below the vascular "polyps."

The *en face* OCT images on the right side of each pair show the full anatomic extent of the membrane and surrounding fluid accumulation. Information on the depth-resolved morphology of the retina in these volumes is acquired by switching the system into the B-scan regime to obtain an image such as that shown in Fig. 12(c). This cross section image displays the distorted shape of retinal layers invaded by the vascular membrane growing up from the choroid.

The next case (Fig. 13) demonstrates features of polypoidal choroidal vasculopathy. ICG angiography is particularly effective in imaging these aneurysmal-like dilations of choroidal vessels with associated neovascular complexes. The surrounding RPE elevations and associated serous retinal detachments are better characterized by the C-scan OCT images, which reveal the topographical cross sections in the coronal plane. Corresponding B-scan OCT images best demonstrate the depth of the serous elevations, as in Fig. 13(c).

Integration of ICG angiography with OCT provides a more complete description of leakages and lesions. In these image pairs, blood vessels are well defined in the ICG images while inconsistently revealed within the OCT images. At the same time, the depth resolution in the ICG channel is low (∼1 mm) and morphology cannot be assessed accurately. Therefore, we believe that such a system will have valuable applications by melding together the different and often complementary information supplied by the two channels. Regions of leakage, visible in the ICG image, can be selectively targeted by acquiring B-scan cross sections in the OCT channel.

7 Conclusions

We demonstrated the simultaneous operation of two separate acquisition and display channels—OCT and fluorescence—in

a retinal imaging system. The pixel-to-pixel correspondence inherent in the design of this system enables an integrated and potentially more accurate analysis of the morphology and functions of the retina and choroids than is currently possible.

In these images, blood vessels are well defined in the ICG images while barely seen in the OCT images. At the same time, the depth resolution in the ICG channel is low (~1 mm) and morphology cannot be assessed accurately. Therefore, we believe that such a system will have valuable applications by melding together the different and often complementary information supplied by the two channels. Regions of leakage, visible in the ICG image can be minutely assessed in the OCT channel, let alone the advantage of one event eye irradiation and elimination of the errors inherent when images provided by two different imaging instruments are correlated.

The research has shown the problems raised by combining the two different imaging technologies, which the present research program should address together with the limitations of the first prototype. The optimization has minimized the deterioration of the depth sampling profile due to the CS in the OCT path, while finding the best trade-off between the strength of signal in the OCT and fluorescence channel. Coefficients were defined to quantify the performances of the system to guide the optimization. These can also be used to assess the system comparatively with angiography systems using lasers.

The operation at 2 Hz in the C-scan regime and at 1 Hz in the B-scan regime is too low not only for the eye movements but the acquisition of fluorescent images must be done fairly promptly due to the fast ICG disappearance rate from the blood stream. Therefore, more work is required to realize the full benefit of the simultaneous presentation of the OCT and ICG images.

References

1. A. Scheider and C. Schroedel, "High resolution indocyanine green angiography with laser scanning ophthalmoscope," *Am. J. Ophthalmol.* **108**, 458–459 (1989).
2. L. A. Yanuzzi, R. W. Flower, and J. S. Slatker, Eds., *Indocyanine Green Angiography*, Mosby, St Louis (1997).
3. W. J. Geeraets and E. R. Berry, "Ocular spectral characteristics as related to hazards from lasers and other light sources," *Am. J. Ophthalmol.* **66**, 15–20 (1968).
4. D. Huang, E. A. Swanson, C. P. Lin, J. S. Schuman, W. G. Stinson, W. Chang, M. R. Hee, T. Flotte, K. Gregory, C. A. Puliafito, and J. G. Fujimoto, "Optical coherence tomography," *Science* **254**, 1178–1181 (1991).
5. C. Puliafito, *Optical Coherence Tomography of Ocular Diseases*, SLACK Inc., Thorofare, NJ (1996).
6. W. Drexler, "Ultrahigh resolution optical coherence tomography," *J. Biomed. Opt.* **9**, 47–74, (2004).
7. H. W. Lim and N. A. Sotter, *Clinical Photomedicine*, Marcel Dekker, New York (1993).
8. M. L. J. Landsman, G. Kwant, G. A. Mook, and W. G. Zijlstra, "Light-absorbing properties, stability, and spectral stabilization of indocyanine green," *J. Appl. Physiol.* **40**, 575–583 (1976) and http://omlc.ogi.edu/spectra/icg/land-plasma.html.
9. R. C. Benson and H. A. Kues, "Fluorescence properties of indocyanine green as related to angiography," *Phys. Med. Biol.* **23**, 159–163 (1978).
10. A. G. Podoleanu and D. A. Jackson, "Combined optical coherence tomograph and scanning laser ophthalmoscope," *Electron. Lett.* **34**, 1088–1090 (1998).
11. G. M. Dobre, A. G. Podoleanu, and R. B. Rosen, "Simultaneous optical coherence tomography—indocyanine green dye fluorescence imaging system for investigations of the eye's fundus," *Opt. Lett.* **30**, 58–60 (2005).
12. A. G. Podoleanu, J. A. Rogers, and D. A. Jackson, "Three dimensional OCT images from retina and skin," *Opt. Express* **7**, 292–298 (2000).
13. A. G. Podoleanu, G. M. Dobre, and D. A. Jackson, "*En-face* coherence imaging using galvanometer scanner modulation," *Opt. Lett.* **23**, 147–149 (1998).
14. A. G. Podoleanu, G. M. Dobre, R. G. Cucu, R. Rosen, P. Garcia, J. Nieto, D. Will, R. Gentile, T. Muldoon, J. Walsh, L. A. Yannuzzi, Y. Fisher, D. Orlock, R. Weitz, J. A. Rogers, S. Dunne, and A. Boxer, "Combined multiplanar optical coherence tomography and confocal scanning ophthalmoscopy," *J. Biomed. Opt.* **9**, 86–93 (2004).
15. R. H. Webb, "Scanning laser ophthalmoscope," in *Noninvasive Diagnostic Techniques in Ophthalmology*, B. R. Masters, Ed., pp. 438–450, Springer-Verlag, New York (1990).
16. W. Drexler, U. Morgner, R. K. Ghanta, F. X. Kartner, J. S. Schuman, and J. G. Fujimoto, "Ultrahigh-resolution ophthalmic optical coherence tomography," *Nat. Med. (N.Y.)* **7**, 502–507 (2001).
17. G. R. Cherrick, S. W. Stein, C. M. Leevy, and C. S. Davidson, "Indocyanine green: observations of its physical properties, plasma decay, and hepatic extraction," *J. Clin. Invest.* **39**, 592–600 (1960).
18. J. P. Villeneuve, R. Huot, D. Marleau, and P. M. Huet, "Estimation of hepatic blood flow with indocyanine green: comparison between the continuous infusion and single injection method," *Am. J. Gastroenterol.* **77**, 233–237 (1982).